Chapter 8

Residual stress distribution in multiaxially forged Fe-30Mn-9Al-0.8C low-density steel through experimentation and numerical simulation

8.1 Introduction

Residual stresses represent self-equilibrating internal stresses inherently present in manufactured components, existing independently of external forces and constraints [112]. The residual stresses in materials can be found by using a variety of techniques, including layer removal, X-ray and neutron diffraction, hole drilling, and more [114-115]. XRD is a widely used non-destructive method for residual stress measurement. This method works exceptionally well for measuring macroscopic stresses under different loading scenarios, offering a unique chance for the thorough study of deformation mechanisms and changes in internal stress in polycrystalline materials. The stress tensor, averaged over the measured volume, is assumed to produce a linear distribution of d vs. $\sin^2\psi$ in order to calculate stress from the strain data that has been recorded. This linearity manifests when there is no detectable in-depth stress gradient inside the material depth. However, significant non-linearities can appear in cold-formed polycrystalline materials, as evidenced by oscillating patterns in the d vs. $\sin^2\psi$ plots. Shear stresses are present in these situations normal to the specimen surface, which explains the elliptical trajectory of the d vs $\sin^2\psi$ distribution.

8.2 Results and Discussion

8.2.1 Residual stress results by X-ray diffraction

Figures 46a-c, Figs. 47a-c, Figs. 48a-c and Figs. 49a-c give d vs $\sin^2\psi$ curves (at $\Phi = 0^\circ$& 180°, 45° & 225° and 90° & 270°) for MAF-0, MAF-1, MAF-3, and MAF-5, respectively for the

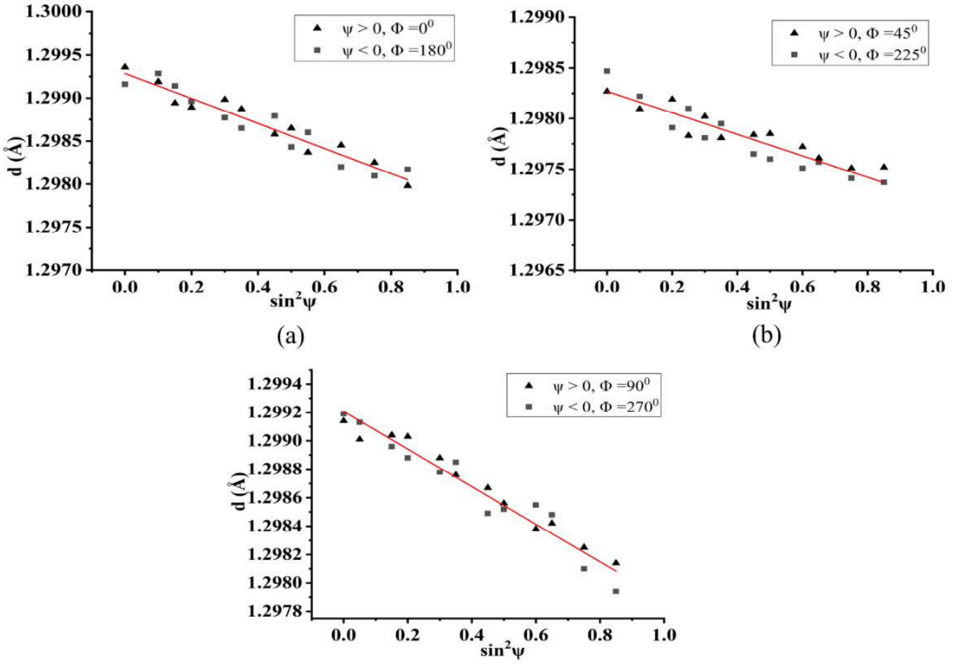

(a) (b)

(c)

Fig. 46: d vs. $\sin^2\psi$ plots for MAF-0 at (a) $\Phi = 0^0$ & 180^0, (b) $\Phi = 45^0$ & 225^0, and (c) $\Phi = 90^0$ & 270^0

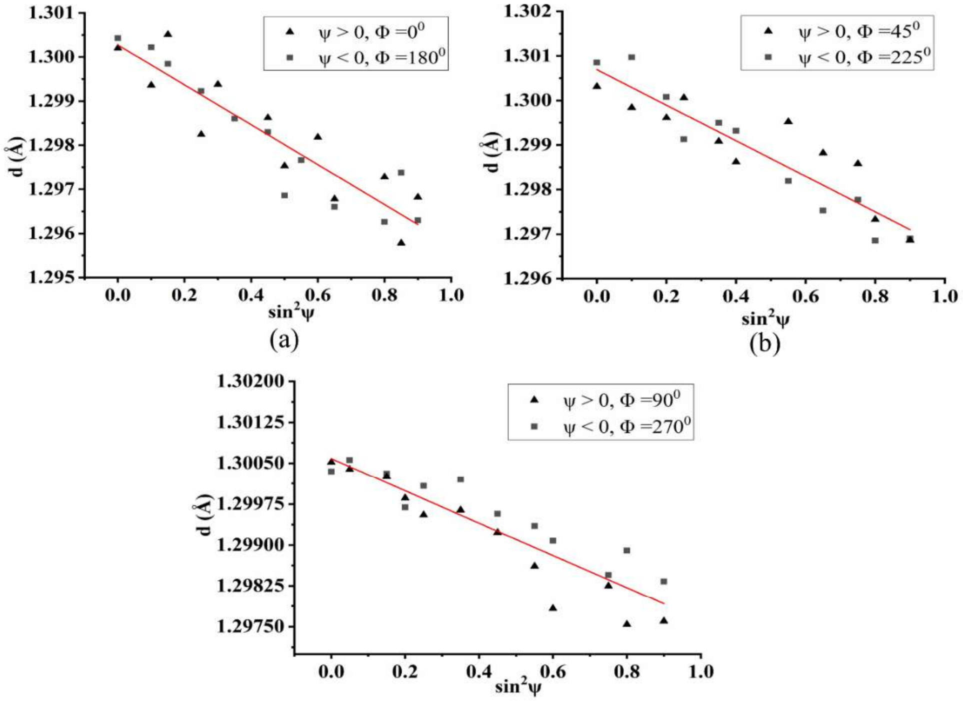

(a) (b)

(c)

Fig. 47: d vs. $\sin^2\psi$ plots for MAF-1 at (a) $\Phi = 0^0$ & 180^0, (b) $\Phi = 45^0$ & 225^0, and (c) $\Phi = 90^0$ & 270^0.

the diffracting plane of (311). Figs. 46-49. clearly display "ψ-splitting" in d values for all the selected Φ angles for all the analysed samples. Therefore, shear stresses exist for all the materials. As a result, the residual stress components are calculated by using a triaxial state of stress analysis for all the materials.

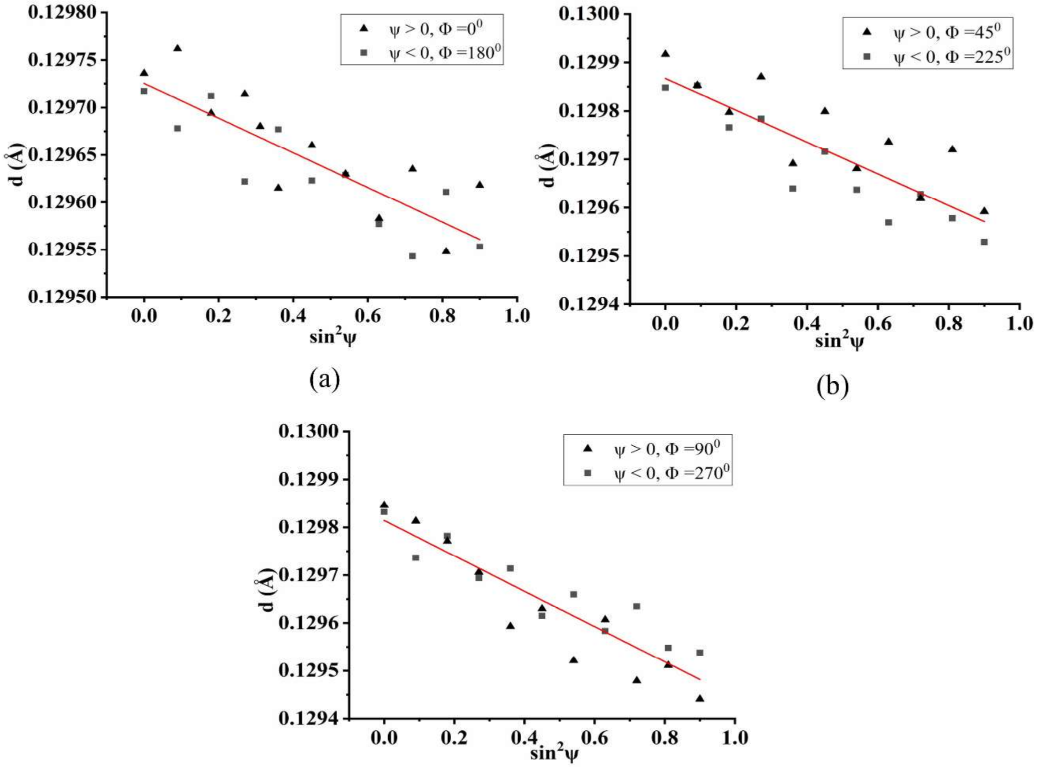

(a) (b) (c)

Fig. 48: d vs. $\sin^2\psi$ plots for MAF-3 at (a) $\Phi = 0^0$ & 180^0, (b) $\Phi = 45^0$ & 225^0 and (c) $\Phi = 90^0$ & 270^0.

After Φ rotation of 180°, ψ+ becomes pseudo ψ-. Here, ψ is taken positive (i.e. ψ+) for Φ from 0°-180°, but ψ is taken pseudo negative (i.e. ψ-) for complementary Φ or Φ +180°. For a triaxial state of residual stress analysis of MAF-0, the strain value, $\varepsilon_{\Phi\psi+}$ & $\varepsilon_{\Phi\psi-}$ are calculated using Eq. (4) and data from plots of Fig. 46a-c at Φψ+ and Φψ- for both positive and negative ψ, respectively. Here "d" values for ψ+ tilting are taken from d vs. $\sin^2\psi$ plots at Φ=0°,45°, and 90° given by Figs. 46a-c. On the other hand, "d" values for ψ-tilting are taken from d vs. $\sin^2\psi$ plots at Φ=180°, 225°, and 270°, which are given by Figs. 46a-c. The average macrostrain (a_1) and the mean macrostrain (a_2) are defined as per Eqs. (24) and (25), respectively [118].

$$a_1 = \frac{1}{2}\left[\varepsilon_{\Phi\Psi+} + \varepsilon_{\Phi\Psi-}\right] = \left\{\frac{d_{\Phi\Psi+}+d_{\Phi\psi-}}{2d_0} - 1\right\} \tag{24}$$

$$a_2 = \frac{1}{2}\left[\varepsilon_{\Phi\psi+} - \varepsilon_{\Phi\psi-}\right] = \frac{d_{\Phi\psi+}-d_{\Phi\psi-}}{2d_0} \tag{25}$$

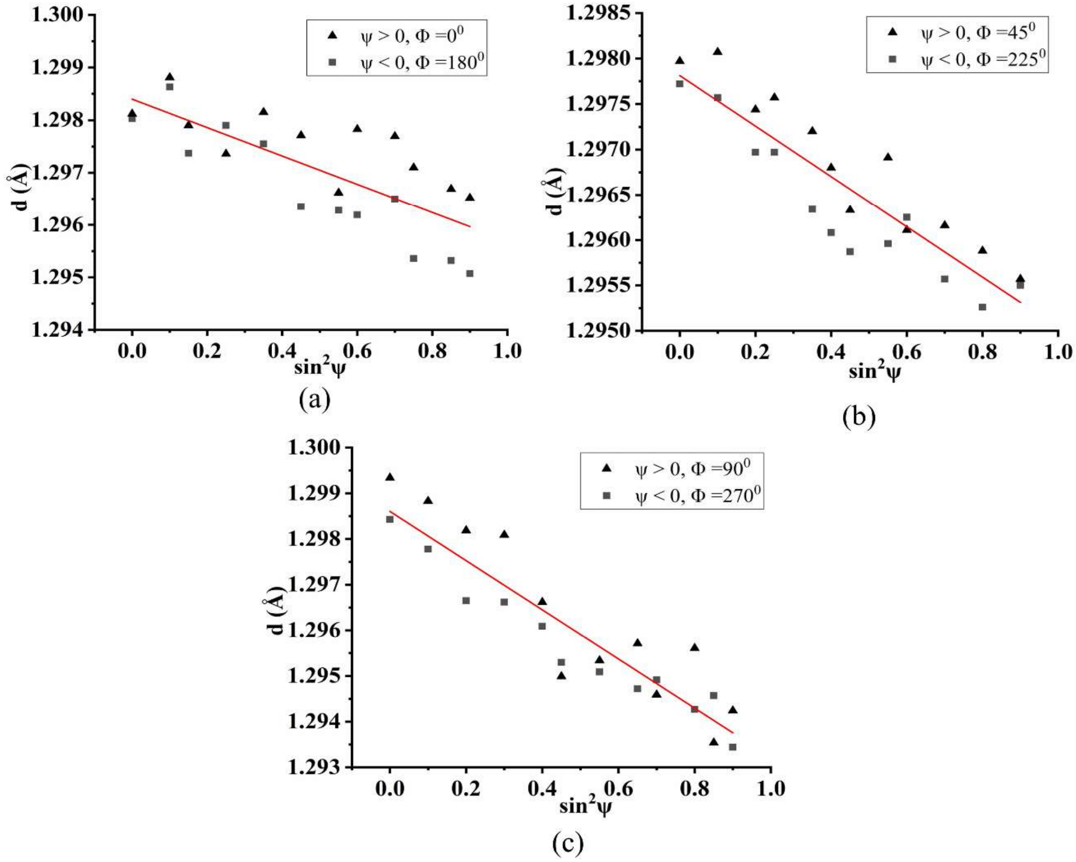

(a) (b) (c)

Fig. 49: d vs. $\sin^2\psi$ plots for MAF-5 at (a) Φ =0^0 & 180^0, (b) Φ =45^0 & 225^0 and (c) Φ =90^0 & 270^0.

Values of a_1 and a_2 are calculated using Equations (24) and (25), respectively, from the measured strain values of, $\varepsilon_{\Phi\Psi+}$ & $\varepsilon_{\Phi\Psi-}$.

A correlation of a_l with stress components is obtained using Eqs. (9) and (24), which is given by Eq. (26). Similarly, a correlation of a_2 with stress components is obtained using Eq. (9) and Eq. (25), which is given by Eq. (27).

$$a_1 = \frac{1+\nu}{E}\{\sigma_{11}cos^2\Phi + \sigma_{12}\,sin2\Phi + \sigma_{22}sin^2\Phi - \sigma_{33}\}sin^2\psi$$

$$+\frac{1+\nu}{E}\,\sigma_{33} - \frac{\nu}{E}(\sigma_{11} + \sigma_{22} + \sigma_{33}) \qquad (26)$$

$$a_2 = \frac{1+\nu}{E}\{\sigma_{13}cos\Phi + \sigma_{23}\,sin\Phi\}\,sin|2\psi| \qquad (27)$$

From the calculated a_l estimated from the measured strain values, $\varepsilon_{\Phi\Psi+}$ & $\varepsilon_{\Phi\Psi-}$, plots of a_l vs $sin^2\psi$ are made at Φ=0° & 180°, Φ=45° & 225°, and Φ=90° & 270°, for MAF-0, which are given by Figs. 50 a-c. Similarly, the calculated a_2 estimated from the measured strain values of $\varepsilon_{\Phi\Psi+}$ & $\varepsilon_{\Phi\Psi-}$, plots of a_2 vs $sin|2\psi|$ are made at Φ=0° & 180° and Φ=90° & 270° for MAF-0, which are given by Figs. 50 d-e.

Figures 50a-c are approximately linear plots which have slopes of m_0, m_{45}, and m_{90}, respectively at Φ=0°, 45° and 90°, and all three plots have almost the same intercept value c of $2.2\text{x}10^{-4}$. Figures 50d-e are also approximately linear plots which have slopes of n_0 and n_{90} respectively, at Φ=0° and 90°.

Eq. (26) is a linear equation between a_l vs $sin^2\psi$, the slope of which can be equated with m_0, m_{45}, m_{90} that can be represented by Eqs. (28-30) and intercept of which can be equated with c that can be represented by Eq. (31).

Eq. (27) is also a linear equation between a_2 vs $sin|2\psi|$. The slope can be equated with n_0 and n_{90}, and that can be represented by Eqs. (32-33).

$$m_0 = \frac{1+\nu}{E}\{\sigma_{11}cos^2\Phi + \sigma_{12}\,sin2\Phi + \sigma_{22}sin^2\Phi - \sigma_{33}\} \qquad (28)$$

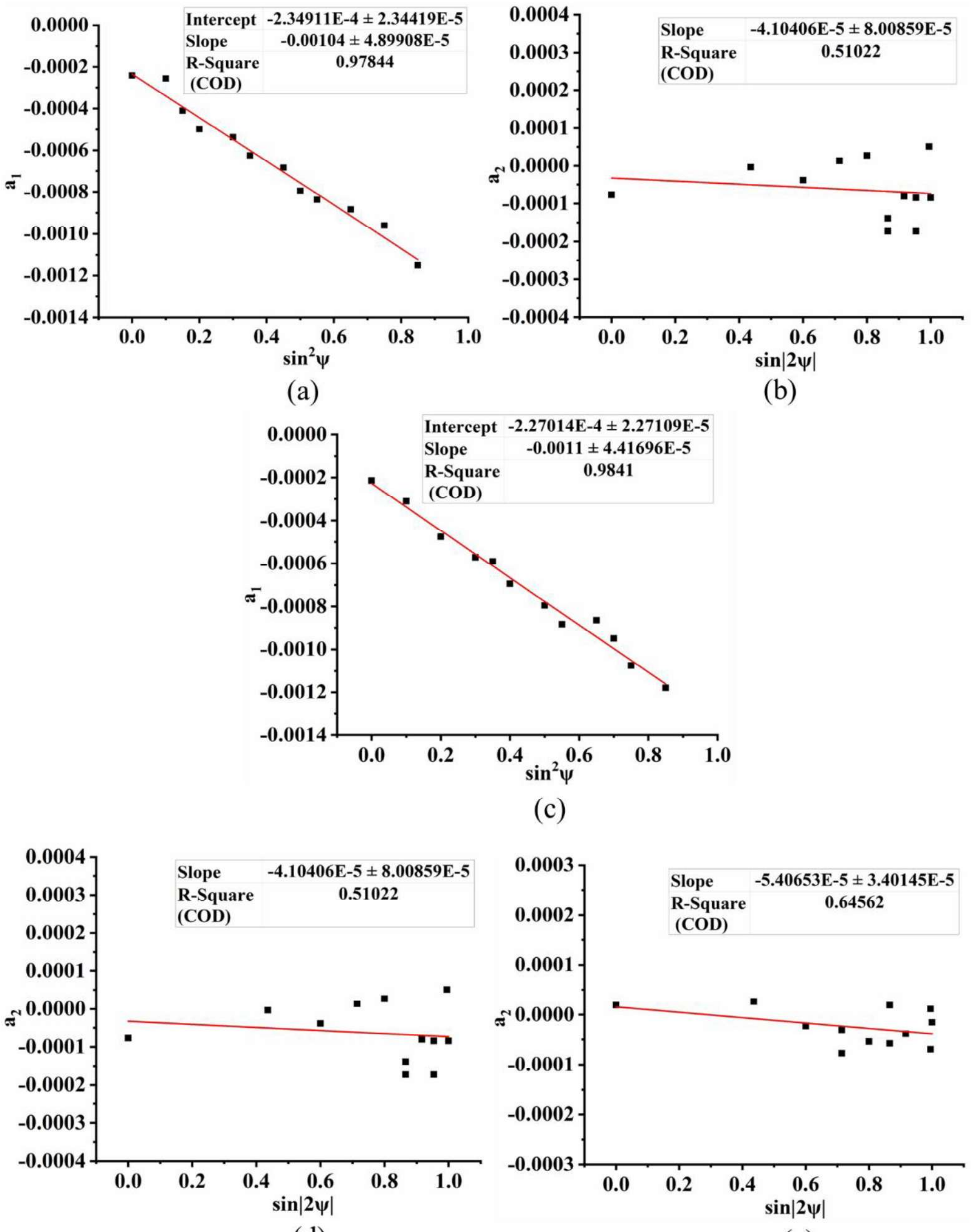

(a) (b) (c) (d) (e)

Fig. 50: a$_1$ vs $sin^2\psi$ plots at (a) Φ=0° &180°, (b) Φ=45° & 225°, and (c) Φ=90° & 270° and a$_2$ vs $sin|2\psi|$ plots at (d) Φ=0° &180°, and (e) Φ=90° & 270° for MAF-0 sample.

$$m_{45} = \frac{1+\nu}{E}\{\sigma_{11}cos^2\Phi + \sigma_{12}\,sin2\Phi + \sigma_{22}sin^2\Phi - \sigma_{33}\} \quad (29)$$

$$m_{90} = \frac{1+\nu}{E}\{\sigma_{11}cos^2\Phi + \sigma_{12}\,sin2\Phi + \sigma_{22}sin^2\Phi - \sigma_{33}\} \quad (30)$$

$$c = \frac{1+\nu}{E}\sigma_{33} - \frac{\nu}{E}(\sigma_{11} + \sigma_{22} + \sigma_{33}) \tag{31}$$

$$n_0 = \frac{1+\nu}{E}\{\sigma_{13} cos\Phi + \sigma_{23}\, sin\Phi\} \tag{32}$$

$$n_{90} = \frac{1+\nu}{E}\{\sigma_{13} cos\Phi + \sigma_{23}\, sin\Phi\} \tag{33}$$

Taking $\nu = 0.3$ and $E = 160$ GPa, using slopes (m_0, m_{45}, m_{90}) and intercept c of Figs. 50a-c, numerical values of normal stresses σ_{11}, σ_{22}, σ_{33} and shear stress σ_{12}, are found by solving Eqs. (29-31). Using slopes of n_0 and n_{90}, from Figs. 50d-e, Eqs. (32-33) are solved for the numerical values of shear stresses of σ_{23}, and σ_{13}. The estimated normal and shear residual stress components for MAF-0 are given in Table 17.

Similarly, from the calculated a_1 estimated from the measured strain values of, $\varepsilon_{\Phi\Psi+}$ & $\varepsilon_{\Phi\Psi-}$, plots of a_1 vs $sin^2\psi$ are made at Φ=0° & 180°, Φ=45° & 225°, and Φ=90° & 270°, for MAF-1, MAF-3, and MAF-5 which are given by Figs. 51a-c, Figs. 52a-c and Figs.53a-c, respectively. The calculated a_2 estimated from the measured strain values of $\varepsilon_{\Phi\Psi+}$ & $\varepsilon_{\Phi\Psi-}$, plots of a_2 vs $sin|2\psi|$ are made at Φ=0° & 180°, and Φ=90° & 270°, for MAF-1, MAF-3, and MAF-5 which are given by Figs. 51d-e, Figs. 52d-e and Figs.53d-e, respectively.

Similarly, taking $\nu = 0.3$ and $E = 160$ GPa, using slopes (m_0, m_{45}, m_{90}) and intercept c of Figs. 51a-c, Figs. 52a-c & Figs.53a-c, numerical values of normal stresses σ_{11}, σ_{22}, σ_{33} and shear stress σ_{12}, are found by solving Eqs. (13-16) for MAF-1, MAF-3 and MAF-5. Using slopes of n_0 and n_{90}, from Figs. 51d-e, Figs. 52d-e and Figs.53d-e, Eqs. (32-33) are solved for the numerical values of shear stresses of σ_{23}, and σ_{13} for MAF-1, MAF-3 and MAF-5. The estimated normal and shear residual stress components for MAF-1, MAF-3 and MAF-5 are also given in Table 17.

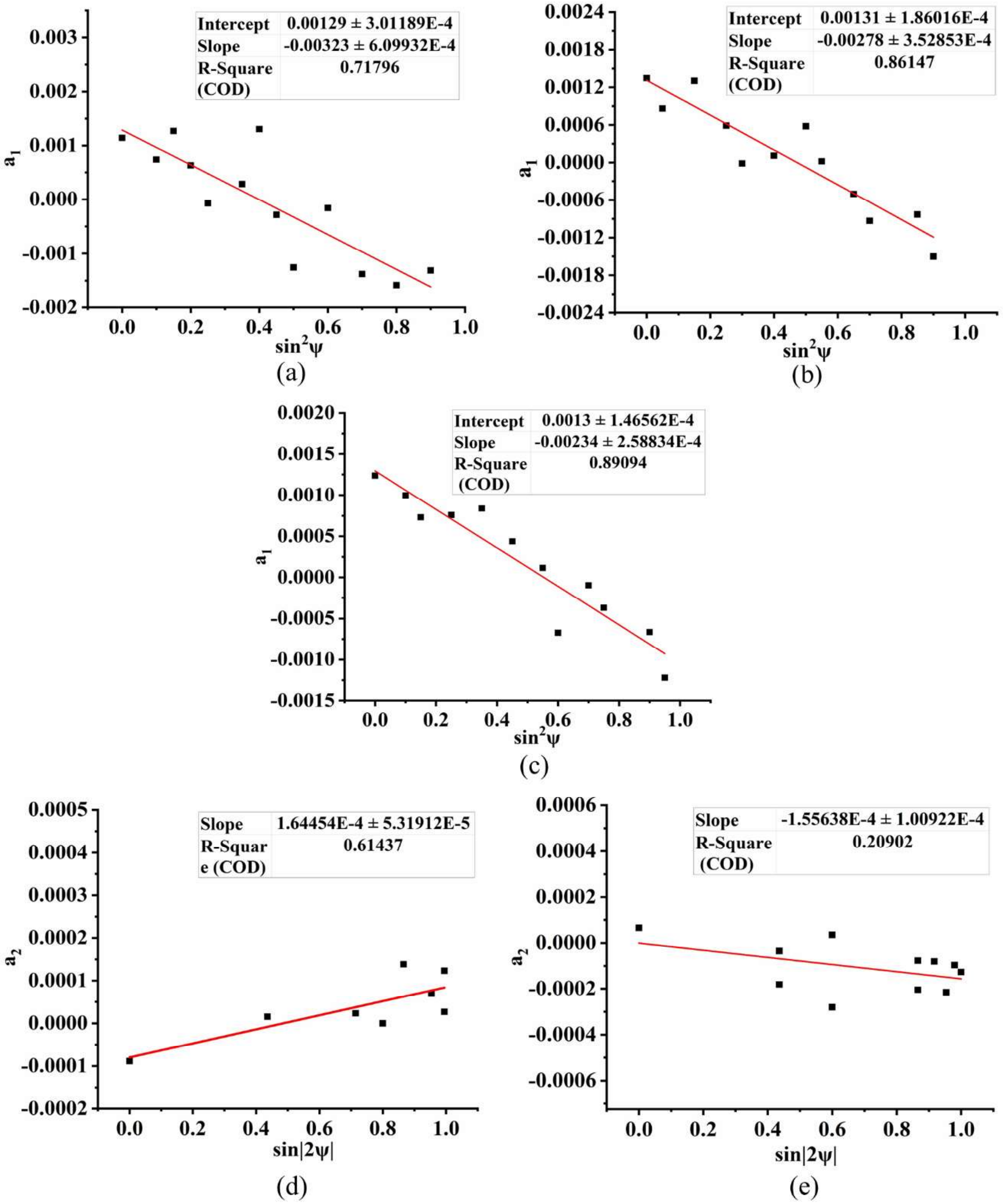

Fig. 51: a_1 vs $sin^2\psi$ plots at (a) Φ=0° &180°, (b) Φ=45° & 225°, and (c) Φ=90° & 270° and a_2 vs $sin|2\psi|$ plots at (d) Φ=0° &180°, and (e) Φ=90° & 270° for MAF-1 sample.

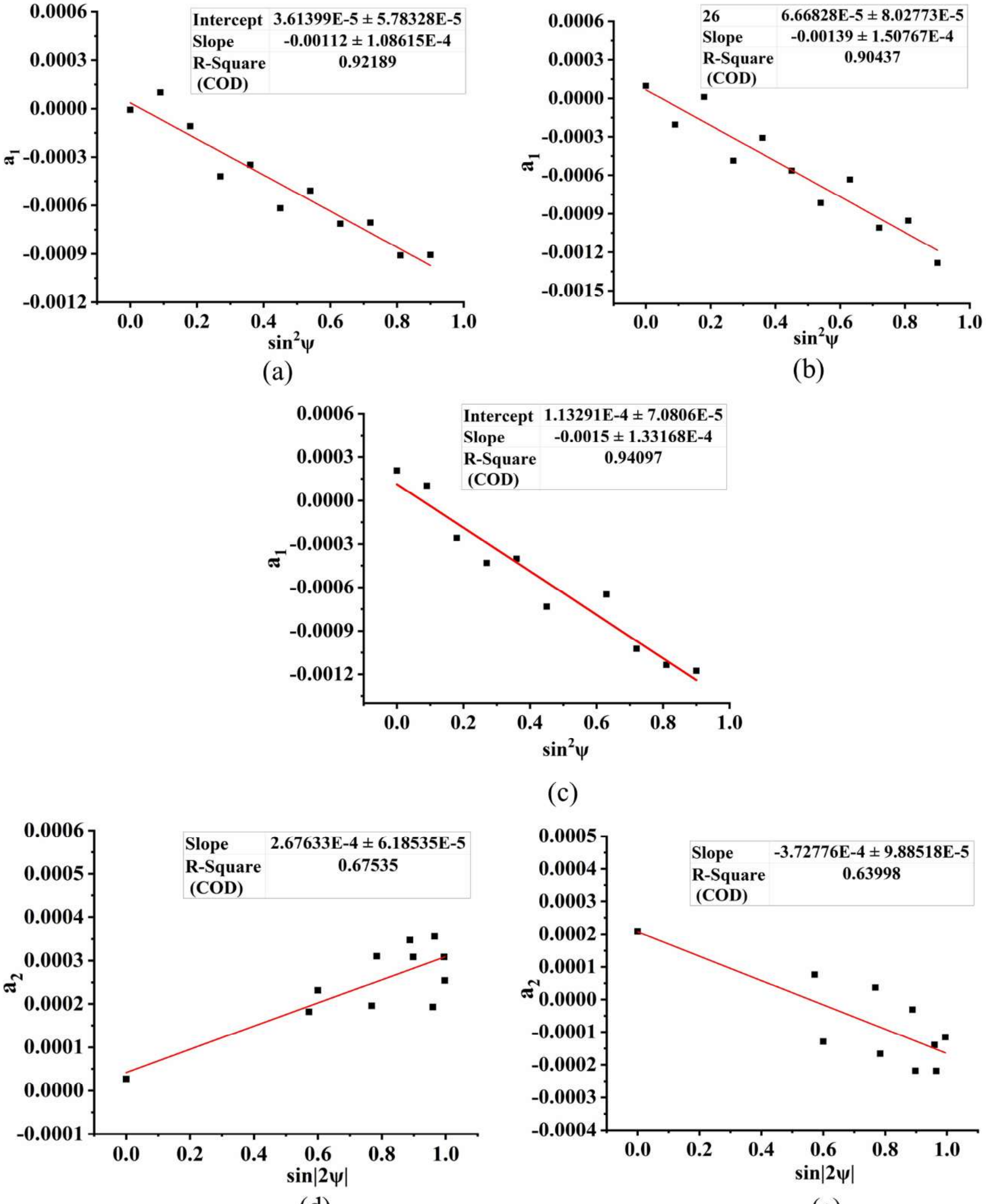

(a) (b) (c) (d) (e)

Fig. 52: a_1 vs $sin^2\psi$ plots (a) Φ=0° & 180°, (b) Φ=45° & 225°, and (c) Φ=90° & 270° and a_2 vs $sin|2\psi|$ plots (d) Φ=0° & 180°, and (e) Φ=90° & 270° for MAF-3 sample.

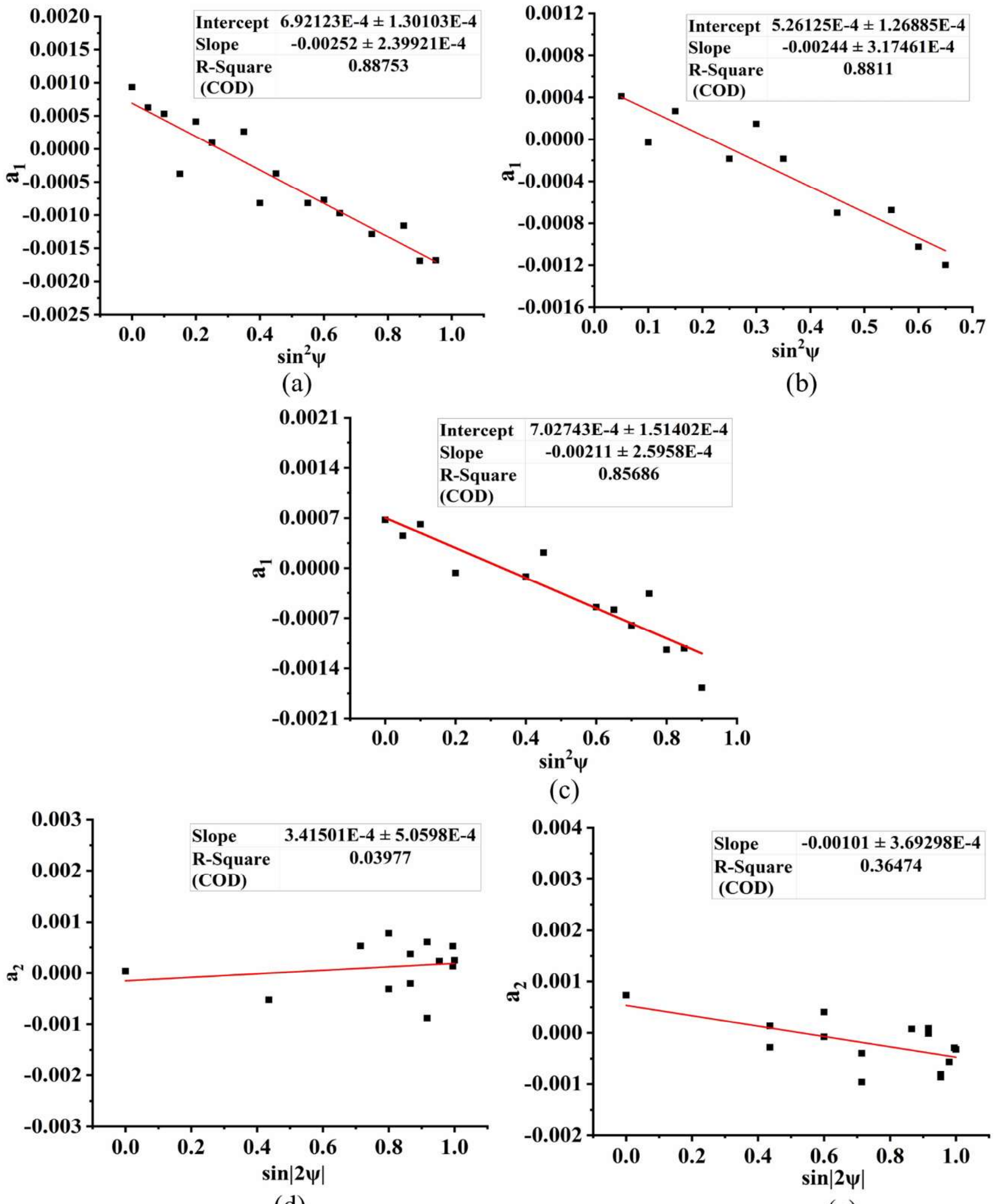

(a) (b) (c) (d) (e)

Fig. 53: a_1 vs $sin^2\psi$ plots (a) Φ=0° & 180°, (b) Φ=45° & 225°, and (c) Φ=90° & 270° and a_2 vs $sin|2\psi|$ plots (d) Φ=0° & 180°, and (e) Φ=90° & 270° for MAF-5 sample.

Both Fig. 50d and Fig. 50e show a negative slope, which indicates σ_{13}, and σ_{23} are compressive in nature for MAF-0, but the slopes of Fig. 51d, Fig. 52d and Fig. 53d are positive. Therefore, σ_{13}, values for MAF-1, MAF-3 and MAF-5 are positive or tensile in nature.

The deformation experienced by the material during each pass is non-uniform, resulting in the development of triaxial stresses within the workpiece. The nature of stresses on normal and shear stresses are demonstrated through the slopes and ψ-splitting at various +/- psi angles and at different phi angles. The degree of $\sin^2\psi$ splitting directly affects the shear stress magnitude.

Table 17: Measured residual stress components at the top surface of the workpiece.

Type of samples	σ_{11} (MPa)	σ_{22} (MPa)	σ_{33} (MPa)	σ_{12} (MPa)	σ_{23} (MPa)	σ_{13} (MPa)
MAF-0	-109	-26	18	27	5	-6
MAF-1	-390	-280	-7.5	0	-19	20
MAF-3	-349	-396	-212	10	-46	33
MAF-5	-410	-460	-151	81	-123	41

8.2.2 Residual stress results by finite element method

The distribution of the residual stress during MAF obtained by FEM is shown in Fig. 54 with the number of MAF passes. In order to illustrate the distribution of the residual stresses properly, the deformed model is cut by the middle cross-sectional plane. Thus, the half part of the deformed model reveals the primary stress (S_{11} or σ_{11}) in the flow direction, secondary stress (S_{22} or σ_{22}) in the constrained direction, and normal stress (S_{33} or σ_{33}) in the pressing direction, Figs. 54a-c. Values of residual stress at the top surface, at the middle of the top surface and the inner core, and at the inner core region are denoted to show the variation of stresses with the depth. At the top surface, all the normal stresses are

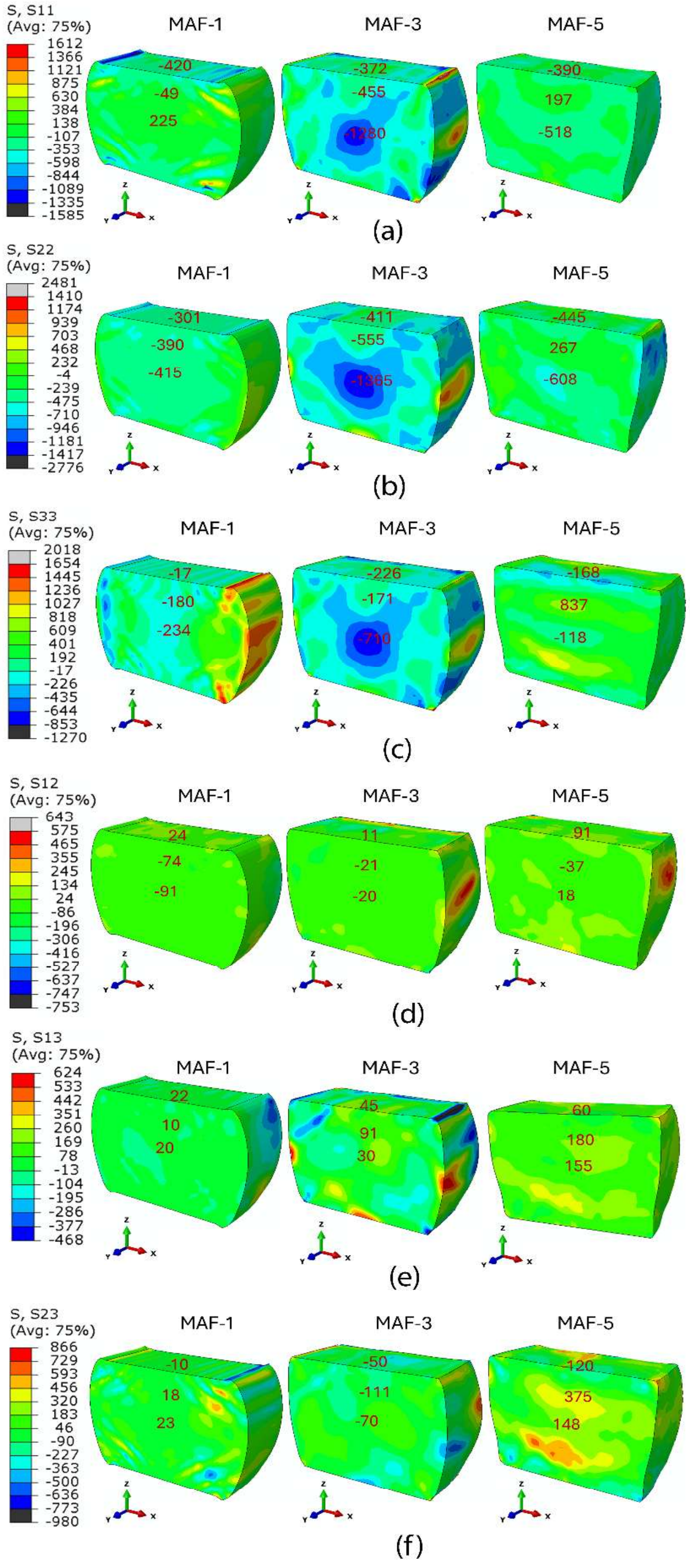

Fig. 54: Distribution of residual stress (in MPa) for various passes. (a), (b), (c), (d), (e), and (f) correspond to σ_{11}, σ_{22}, σ_{33}, σ_{12}, σ_{23}, and σ_{13}, respectively.

compressive (Figs. 54a-c), while the shear stresses are tensile or compressive with MAF passes (Figs. 54d-f). The FEM results are

consistent with the residual stress obtained via XRD measurement (Table 17). Though there are some variations, they are within acceptable limits. The residual stress at the surface is influenced by the frictional effect during the forging operation. However, it is not necessarily consistent across all operations. This variability in the frictional effect can lead to deviations from the simulated stress.

Moreover, the residual stress observed towards the centre indicates that σ_{22} and σ_{33} are compressive and steadily increase from the surface towards the centre. Conversely, σ_{11} is compressive at the surface following MAF-1 (Fig. 54a), transitioning to tensile stress from the surface to the inner core. Subsequently, σ_{11} becomes compressive in the inner core following MAF-3 and MAF-5. Moreover, after MAF-3, the normal residual stresses exhibit maximum compressive behaviour at the inner core. Residual shear stresses exhibit lower magnitudes compared to the normal residual stresses (Figs. 54d-f) and demonstrate an unpredictable trend. Meanwhile, the normal stresses undergo a transition to tensile behaviour between the top surface and inner core after five passes.

8.2.3 Effect of multiaxial loading on residual stress

Initially, at solution-treated condition (MAF-0), the residual stresses are generated due to biaxial hot forging for about 60% reduction in height at the temperature range 1200°C-900°C and the thermal contraction during quenching. Li et al. display that the deformation of Fe–27Mn–11.5Al– 0.95C at 900°C for strain rate 1 s-1 initiates nucleation of dynamically recrystallized (DRXed) grains, and with increasing temperature and decreasing strain rate DRX is favored [205]. Wan et al. show that hot deformation of Fe-25.14Mn-10 Al-1.46 C-0.053 Nb recrystallizes grains dynamically in the temperature and strain rate combination of 950-1000°C/0.01–0.1 s−1 and 1050–1100 °C/1–10 s−1 [206].

Lu et al. deform Fe–27.34Mn–8.63Al–1.03C alloy at the temperature range of 1010-1100°C and strain rate of 0.01s-1 and found a significant amount of grains got recrystallized dynamically [207]. All the above studies confirm that the selected alloy is not completely recrystallized by the hot deformation and solutionising conditions. Therefore, some residual stress is expected in the MAF-0 sample (Table 3). The initial microstructure of the material and the manufacturing process play a significant role in the generation of residual stress [208]. WQ can also lead to the generation of residual stress [209].

Equivalent strain gradually increases linearly in all three directions during the MAF process, moving from the sample's exterior to its core, with its magnitude increasing proportionally to the number of passes and the friction coefficient [210]. After the samples are deformed by MAF, significant residual stress is observed throughout the depth. In contrast to SPD methods like equal channel angular rolling and deep rolling [124], [211-212], which solely impart compressive residual stress at the surface and through thickness, MAF induces a more intricate triaxial stress distribution. MAF results in a compressive surface residual stress profile, while the stress state at the centre may be tensile or compressive. Additionally, shear stresses may arise from material heterogeneity, introducing nonuniform microstrains within the material [129].

The various stress states primarily arise from the die geometry. Friction exists between the sample and the punch, as well as between the sample and the die wall. Friction causes less deformation on the outer surface compared to the inner surface. When external force is released, outer surface elastic deformation fully recovers, but tensile residual strain remains on the inner surface in flow direction, while compressive residual strain remains in pressing direction and constrained direction. During MAF-1, the residual strain results in residual stress in corresponding direction. This creates compressive residual stress (σ_{22}) on the outer surface and tensile stress (σ_{22}) in the inner core, transitioning from compression to tension outward to inward (Fig. 54b). Friction between the dies and the deformable sample impede the flow of metal near the contact surface layers, although its impact on the centre of the workpiece, where the maximum strain is developed, is relatively minimal [210]. Bulging is observed in static loading scenarios wherein compressive forces are applied in the loading direction, resulting in material elongation at the center in the flow direction. This phenomenon is visually represented by the deformed shape denoted as 'x' in the material [106]. Upon removal of the applied load, dislocations become locked, leading to the generation of compressive stress both above and below the affected region, while simultaneously causing tensile residual stress at the center. In the other two directions (pressing direction and constrained direction) the material experiences compressive load as well as friction load and the cumulative effect causes compressive residual stress after unloading. This intricate interplay of forces underscores the complex residual stress behaviour exhibited by the material during constrained die forging. However, it is observed that friction significantly influences only up to the third pass, assisting in the generation of compressive residual stress within the material. The tensile residual stress develops between the surface (compressive) and the inner region (compressive) (Fig. 54a-c), indicating a decrease in the role of friction by the 5th pass. In the 6th pass, friction fails to contribute to compression at the surface, leading to material failure due to large tensile stresses at the surface.

8.3.4 Effect of dislocation density on residual stress

From mechanical and metallurgical perspectives, the combination of strain hardening, refined grain size, and enhanced dislocation density obtained through multiple passes of MAF is responsible for the improvement of mechanical properties of Fe-30Mn-9Al-0.8C low-density steel, including yield strength and ultimate tensile strength discussed in chapter 6. Although, in context of residual stress, compressive residual stress increases the global yield strength during deformation at first, but as strain increases through the uniform plastic deformation stage, its contribution decreases because of dislocation density saturation [213].

The evolution of dislocation density at surface is examined by FE simulation using relation between yield strength and dislocation density as depicted in Eq. (22), which shows a constant rise with each MAF pass (Fig. 43b). Front and middle cross-sectional planes are selected here for each pass, Fig. 43b. Initially (1-3 pass), the accumulation of dislocations tends to enhance residual stresses due to the presence of internal micro-strain generated by the dislocations themselves. Dislocations significantly grow throughout the MAF process due to slipping and climbing caused by external forces. These dislocation lines become entangled and accumulate, forming groups of dislocation pile-ups hindered by grain boundaries and impurity atoms. Notably, a considerable accumulation of basal-type dislocations occurs at grain boundaries, leading to pronounced stress concentration in their vicinity. The accumulation of microscopic defects manifests itself as the macroscopic residual stress within the material [214]. Mughrabi's research suggests that dislocation arrangement plays a pivotal role in the generation of deformation-induced long-range internal stresses [215], while Wawszczak et al. find that even minor adjustments in dislocation arrangements can result in significant relaxation of macroscopic residual stresses [30]. In accordance with the aforementioned theory, the Kocks-Mecking model delineates the relationship between stress (σ) and dislocation density (ρ) as follows [216]:

$$\sigma = \sigma_0 + \alpha M G b \sqrt{\rho} \tag{34}$$

Where σ_0, denote the stress constant. Notably, the residual stress exhibits a linear relationship with the square root of dislocation density, suggesting that residual stress diminishes with decreasing dislocation density.

It's important to note that while the FE simulation accounts for the work hardening of the target through the utilization of the J-C rate dependency model, it also integrates the microstructure evolution, particularly the processes of dislocation rearrangement and grain refinement. These factors significantly impact the generation of residual stresses observed during MAF.

The dislocation density of the material increases at the surface and inner core with number of passes as shown in Fig. 43b. This rise is attributed to the introduction of high strain up to 2.3 in five passes, leading to an expected increase in residual stress levels. In the chapter 7, it has been discussed that dislocation density continuously increases with increase in the number of MAF passes, but fraction of low-angle boundaries increases up to MAF-3 and reduces in MAF-5. At high strain level the low-angle boundaries are getting converted to high-angle boundaries. Sub grain rearmament at higher strain level may reduce the residual stress but the effect of grain size on the residual stress is still unexplored. However, the evolution of dislocation density influences the generation of residual stresses and has been confirmed by previous studies [30,39-41]. Thus, the stress decrement experience in the final passes, suggests a potential dislocation rearrangement influenced by the inherent recovery process occurring at the current MAF processing temperature. Higher dislocation densities may initially contribute to increase residual stresses, but their continued evolution can lead to stress relaxation and stabilization within the material.

8.3 Conclusions

In this study solutionized sample of Fe-30Mn-9Al-0.8C low-density steel has undergone 5 passes of MAF at 250^0 C. The XRD method is opted for surface residual stress measurement and a triaxial stress analysis is performed for d vs $\sin^2\psi$ value to determine all the stress components. FEM is selected for studying distribution of residual stresses across the volume. Based on results of the present study, the major conclusions are summarized as follows:

- MAF induces a more intricate triaxial stress distribution due to multiaxial loading and friction from die walls, where friction causes a compressive surface residual stress profile, while the stress state at the centre may vary between tensile and compressive.
- XRD measurements show psi splitting which indicates the presence of shear residual stress. Therefore, a triaxial stress analysis is required to determine the stress tensor in multiaxially forged sample.
- Until MAF-3, friction facilitates the generation of compressive residual stress within the material. However, beyond this strain level, tensile residual stress begins to develop between the surface and the inner core.
- From the computed residual stress tensor, it is observed that normal stresses are predominating as compared to the shear components.
- Compressive residual stress mitigates the crack flow. So, after MAF-3 the forged material should be heat treated to reduce the tensile residual stress so that MAF could be continued for more number of passes.
- The study reveals the pivotal influence of dislocation density on residual stresses, demonstrating its dual effect of initially exacerbating stress and subsequently promoting relaxation as the MAF progresses.